

DOI: 10.1002/adma.200602705

Low-Temperature In Situ Large-Strain Plasticity of Silicon Nanowires**

By Xiaodong Han, Kun Zheng, YueFei Zhang, Xiaona Zhang, Ze Zhang,* and Zhong Lin Wang*

Elastic-plastic and fracture properties are key issues in characterizing materials' mechanical behavior, and they have been extensively studied for over a century for bulk structured materials.^[1–3] Silicon is one of the most important and representative materials for these studies owing to its extremely important applications.^[4,5] Silicon nanowires (NWs) are one of the most important nanostructures used for fabricating various electronic and optoelectronic nanodevices,^[6,7] and they could be a building block for the construction and assembly of functional nanometer-scale systems. Although the electrical and optical properties of Si NWs have been extensively studied, only limited information is available about the structure–mechanical property correlations of Si NWs. This is likely due to the difficulty of carrying out in situ tensile or bending measurements on individual NWs. The elastic-plastic strains retained in NWs can significantly affect their electronic properties by perturbing the band structure or changing the Fermi energy of the nanostructures.^[8] For example, the applied strains of continuous torsion on carbon NTs could result in chirality variation and therefore introduce a distinct conductance oscillation from metallic to semiconductor.^[9] A strain-induced giant piezoresistance effect has also been observed for Si NWs.^[10]

Results of studies of the elastic-plastic behavior of Si NWs are of technological importance. Silicon NWs are a potential candidate for building devices that are to be integrated with microelectronics and microelectromechanical systems (MEMS). They are also an outstanding candidate for con-

structing devices for flexible electronics. Several approaches have been developed to study the mechanical properties of NWs and nanotubes (NTs) based on atomic force microscopy (AFM) at nanometer-scale spatial resolution.^[11,12] The major limitation of AFM measurements is that they are unable to reveal the atomic-scale structural evolution process during the in situ elastic-plastic-fracture process. Transmission electron microscopy (TEM) has been one of the most important and effective tools with a capability of atomic level imaging for investigating the in situ mechanical properties of single NWs and NTs,^[13,14] although ex situ studies have to be carried out.^[15,16] Direct and in situ atomic level imaging during tensile testing is fundamentally important to view and provide true physical insight into the elastic-plastic and fracture processes,^[12,13] but this type of study is challenging experimentally.

In this report, we present in situ TEM observation of the elastic-plastic-fracture processes of a single Si NW recorded at atomic resolution. The study directly shows the strain-induced structural evolution process of Si NWs and its large-strain plasticity (LSP). Our results indicate that the LSP of Si NWs via a brittle-ductile transition originates from a dislocation-initiated amorphization. This behavior is in contrast to the mechanical behavior of bulk Si. Our observation reveals a phenomenon and mechanism of the Si NW mechanics and is fundamentally important for Si-NW-based nanotechnology.

The in situ Si NW elastic, elastic-plastic, and plastic deformation investigations were carried out by ultrahigh-resolution TEM (UHRTEM) by axially extending the Si NWs by means of a mechanical force created by a TEM specimen-supporting grid under electron beam irradiation, as reported in detail elsewhere^[17,18] (also see the Experimental section and Supporting Information, Fig. S1). Figure 1a–d shows a series of images of a single Si NW that was extended by the force created by the shrinkage of the broken colloidal thin film (see Experimental section). A clear plastic deformation was observed at the center of the NW. We did not see an abrupt brittle cleavage crack, instead, the NW transformed from crystalline structure to amorphous at the central region of the axially extended NW. Of the nine Si NW samples (ranging from 15 to 70 nm in diameter) we have studied, all showed a large elastic strain if the NW diameter was below 70 nm, and a large plastic deformation rate was achieved. The strain rate was kept at a level of ca. 10^{-5} s^{-1} . A reduction in diameter as large as 426 % (the ratio of initial diameter over breakpoint diameter as a percentage) and 125 % elongation ratio were obtained at ambient temperature for a NW with an original diameter of

[*] Prof. Z. Zhang, Prof. X. D. Han, K. Zheng, Y. F. Zhang, X. N. Zhang
Institute of Microstructure and Properties of Advanced Materials
Beijing University of Technology
Beijing 100022 (P.R. China)
E-mail: zezhang@bjut.edu.cn
Prof. Z. L. Wang
School of Materials Science and Engineering
Georgia Institute of Technology
Atlanta, GA 30332 (USA)
E-mail: zhong.wang@mse.gatech.edu

[**] This research was supported by the National 973 program under the number 2002CB613500, Beijing Education Committee Program 05102001200501, and Funding Project for Academic Human Resources Development in Institutions of Higher Learning under the Jurisdiction of Beijing Municipality. It was also supported by the program for New Century Excellent Talents in Universities. Supporting Information is available online from Wiley or from the authors.

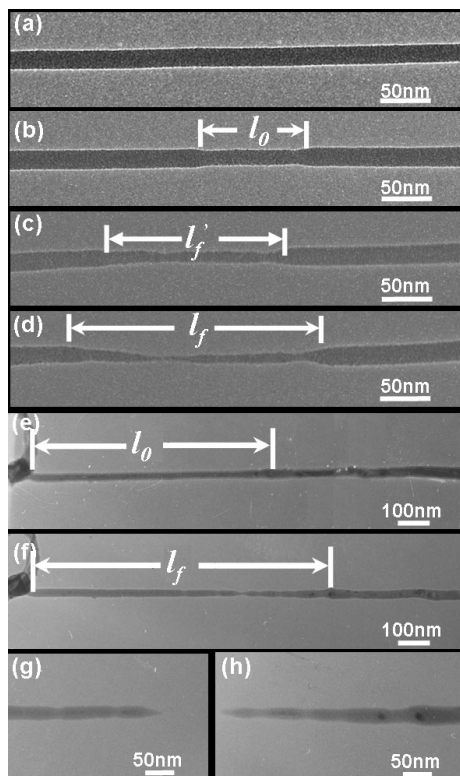


Figure 1. a–d) A Si NW during the in situ application of axial tension. The arrows indicate the corresponding positions of the extended nano-wire throughout the procedure. The original diameter of the Si NW was 26 nm and after plastic elongation the diameter reduced to 6.1 nm. e–h) Another example of extending a Si NW, this time with buckling character. The axial elongation of the Si single-crystalline NWs can be revealed by comparing the corresponding l_0 and l_f .

26 nm, as shown in Figure 1a–d. The series of images in Figure 1e–h shows another example of an axial tensile event of a Si NW, in which buckling of the extended NW was observed, which is similar to the case of carbon NTs.^[16] The diameters of the axially extended NWs were measured prior to and after the plastic elongation. The axial elongation of the Si single-crystalline NWs can be revealed by comparing the corresponding lengths l_0 and l_f in Figure 1.

Table S1 (Supporting Information) summarizes the diameters of the nine extended NWs together with the NWs' orientation. All of the Si NWs have [110] growth direction. The Si NWs' plasticity was evaluated by the diameter reduction ratio r_0/r_f , as a percentage, where r_0 and r_f are the initial and final diameters of the Si NW, respectively. For the NW with $r_0=26$ nm and $r_f=6.1$ nm, a diameter reduction ratio of 426 % and an elongation of 125 % were obtained. This reveals the nature of the LSP. Figure 2 shows a plot of the diameter reduction ratio versus the Si NW diameter. Extrapolation of the plot gave a brittle–ductile transition diameter of around 60 nm for ambient temperature. Reference data^[19] of size-dependent Young's modulus of Si are shown in the same figure. When the NW's diameter is larger than 60 nm, an abrupt brittle fracture can be expected.

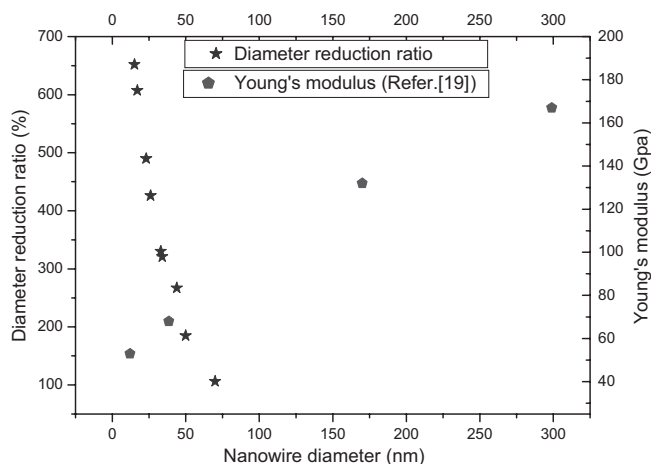


Figure 2. The diameter reduction ratio as a function of nanowire diameter in the case of axial tension at a low temperature close to room temperature. Young's modulus values as a function of diameter are plotted in the same figure for comparison.

We now explore the mechanism of the superplastic deformation of Si NWs through an in situ axial tensile experiment using TEM. Figures 3a and b show low-magnification images of a Si NW being extended at the initial elastic–plastic transition and in the final broken state, respectively. Figure 3c is a HRTEM image of the axially extended Si NW at the initial elastic–plastic transition. Figure 3d is an HRTEM image of the extended Si NW at a later time. Figure 3e is an enlarged HRTEM image taken from the framed region indicated in Figure 3c. Based on the first-order approximation, we may assume that the white dots in the HRTEM images are the projections of Si–Si “dumbbell” atomic pairs,^[20] as in conventional lattice images. The HRTEM image was simulated by multiple-slice theory^[21] and the simulated HRTEM image for the perfect lattice is inserted in Figure 3e, in which every white dot is regarded as a Si–Si dumbbell atomic pair. Tracking the extended Si NW HRTEM image carefully, we find the initial elastic–plastic transition is characterized by activation of plastic dislocations. In Figure 3e, a Burgers vector circuit is drawn around a dislocation and the Burgers vector projection can be directly determined. The dislocation Burgers vector is determined as $(1/2)\langle 110 \rangle$, which is also possibly a projection of $\langle 112 \rangle$, as shown in Figure 3e, a 60° -type dislocation.^[20] This type of dislocation is dominant in this low-temperature plastically deformed Si NW. We suggest that this dislocation was activated on the {111} shuffle planes. Figure 3f shows the two-dimensional (2D) projection of the diamond-type crystalline structure of the Si lattice along [110]. The two types of well-known {111} shuffle and glide planes are indicated in Figure 3f. Theoretically,^[22] the activation of dislocations on the {111} shuffle planes takes less energy (0.1G) than on glide planes (0.35G) at low temperatures, where G is the shear modulus. We have revealed that the dislocations were emitted equivalently on the two $(\bar{1}\bar{1}1)$ and $(\bar{1}\bar{1}\bar{1})$ planes with respect to the external loading force direction and the NW longitude di-

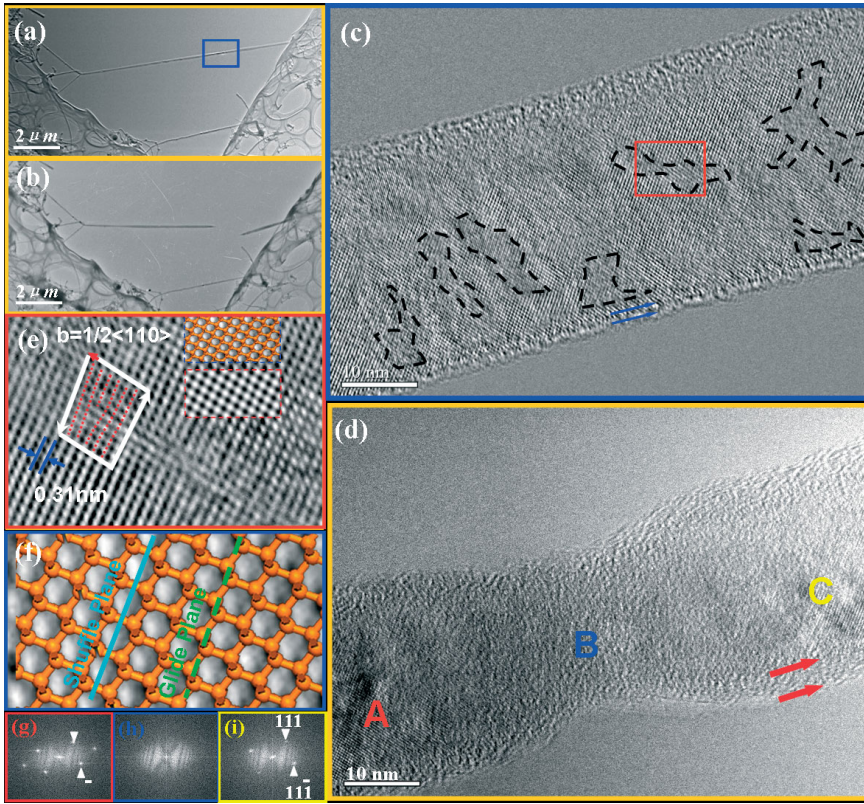


Figure 3. Atomic-level in situ high resolution electron microscopy study of an axially extended Si NW. a,b) Low magnification images prior to and after the Si NW is plastically broken. c) HRTEM image of the Si NW in a status of elastic-plastic transition and prior to severe plastic deformation. d) The same Si NW after large-strain plastic deformation with a neck in the middle of the NW. g–i) The FFT electron diffraction patterns taken from areas A–C in (c), respectively. e) Enlarged HRTEM image taken from the framed region in (c), which indicates the initiation features of plasticity with dislocations. The dislocation structure is highlighted by dotted red lines. A Burgers vector circuit is drawn, indicating a perfect edge dislocation. The simulated HRTEM images of the perfect crystalline lattices and the head–tail connection model are shown as insets. f) Schematic atomic structure of Si atomic lattice projected along the [110] orientation; the shuffle and glide planes are indicated.

rection (see Supporting Information, Fig. S3). Although the dislocation movement from one Peierls potential valley to another was directly revealed in a high temperature experiment in a Si thin film,^[23] our results suggest in this study that the generation of dislocations, rather than increased mobility of dislocations, triggered the initiation of plasticity of Si NWs at room temperature or close to room temperature. In a study of high-pressure-induced plasticity, phase transformations of β -Sn structure^[24] could be induced, however, our present results exclude the occurrence of this type of phase transformation. The availability of high shearing stress and slip systems on the {111} shuffle planes initiated plastic dislocations.

Further, following the initiation of dislocation plasticity, with increased strain, we observed LSP of the axially extended Si NWs at low temperatures. Throughout the whole procedure we did not observe any cracks, even at the atomic scale. The LSP of Si single-crystalline NWs was characterized by the continuous development of disorder in the lattice through emission of dislocations and disordering of crystalline structures

and further amorphization and plastic necking, as shown in Figure 3d. Three fast Fourier transform (FFT) diffraction patterns are shown in Figure 3g–i, corresponding to the areas A–C (Fig. 3d) of the NW, respectively. These indicate that areas A and C are crystalline and B has transformed to a disordered structure. The fraction of the disordered structure with respect to the original crystalline structure varies as a function of distance from the most strained region of the narrowest location of the superplastically deformed Si NW. This indicates that LSP of the axially extended Si NW is a continuous process involving creation of dislocations and disordering of the crystalline lattice, consistent with the theoretical calculation.^[25] We also measured the thickness of the NW surface with disordered structure before (Fig. 3c) and after (Fig. 3d) axial extension. This revealed that, during the process of axially extending the Si NW, the surface disordered lattice area of the Si NW expanded along the radial direction from the original thickness of 3 nm (indicated by two blue arrows) to 7 nm (indicated by two bold red arrows). At the thinnest (most necked) region, the crystalline Si lattice completely transformed to a disordered structure. This observation demonstrates that the plasticity and LSP are surface-effect-triggered phenomena.

It is known that the surface of a Si NW may be covered by a thin oxide layer. It is important to investigate the role possibly played by oxygen diffusion into the lattice, especially in the strained area, during plastic deformation. This study was carried out using in situ electron energy loss spectroscopy (EELS) in an attachment to the transmission electron microscope; data were acquired simultaneously while conducting the axial tensile tests on the Si NW. Figure 4a,b shows two sets of EELS spectra taken from a Si NW before and after superplastic deformation. For each set of EELS analysis, 32 spectra were taken across the diameter of the Si NW; here we have chosen seven of them to demonstrate that neither prior to nor after the superplastic deformation did the SiO_x surface layer diffuse radially into the inner layers of the Si NW, especially not in the highly strained area. Figure 4a shows a series of EELS spectra taken from the Si NW prior to plastic deformation. Figure 4b shows the corresponding EELS spectra taken from the superplastically deformed Si NW with a neck. The corresponding locations at which the EELS spectra were taken are schematically indicated in Figure 4c,d. From comparison of the fine structure of the Si L edge with

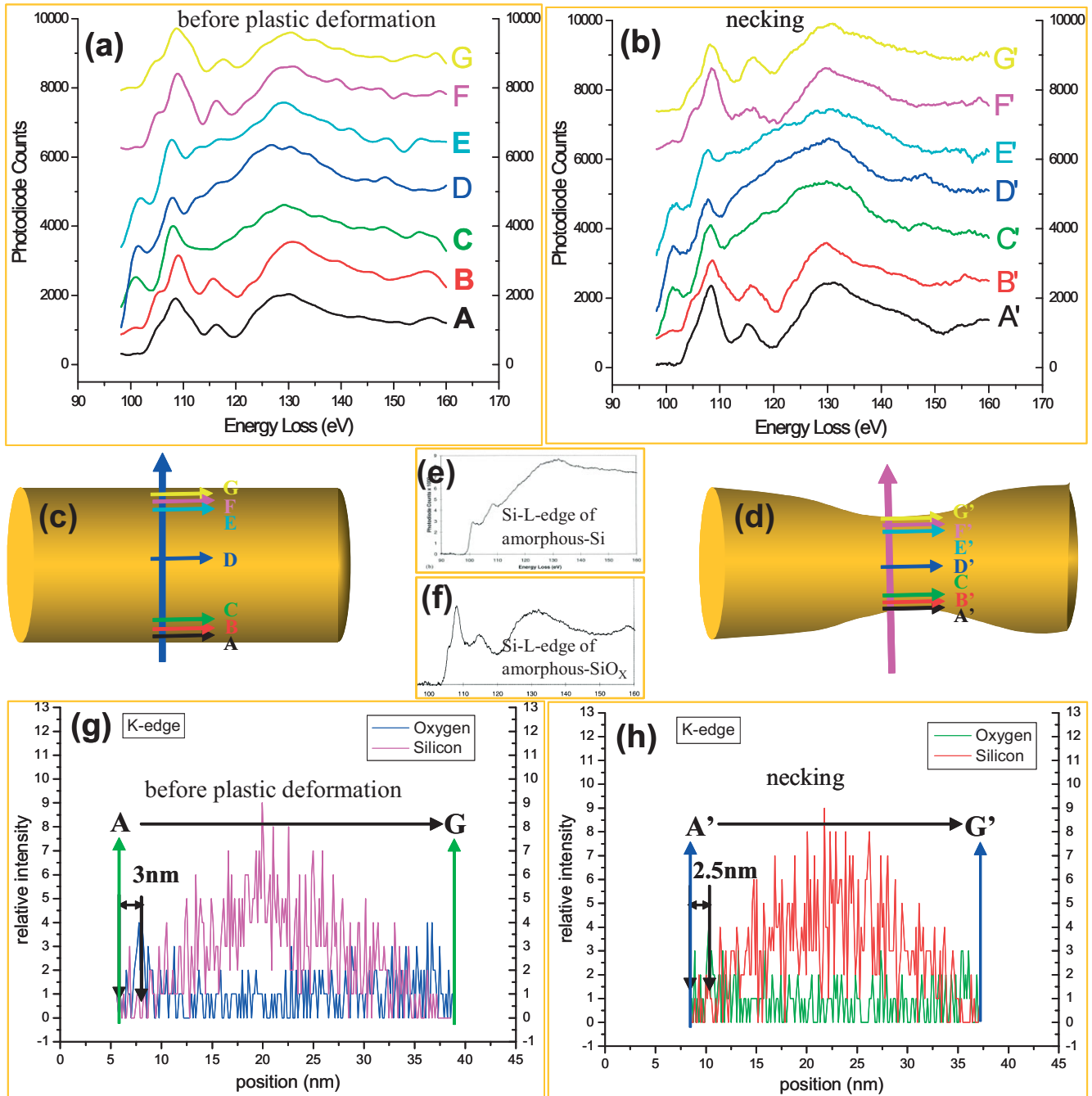


Figure 4. Series of EELS spectra and EDS line scans taken from a Si NW prior to and after large-strain plastic deformation. Both series of EELS spectra were taken across the NW width. a) A series of spectra taken from the Si NW prior to plastic deformation. b) A series corresponding to the NW with a superplastic necking feature. c,d) Schemes of the locations at which the spectra were taken for (a) and (b), respectively. e,f) Reference [26] EELS spectra for the Si L edge of Si and amorphous SiO_x, respectively. g,h) Line scan EDS spectra of elemental oxygen and silicon for the Si NW before and after neck formation. The surface oxygen layer thickness was measured as the distance from the starting position A or A' to the first peak position of oxygen in both oxygen spectra.

standard samples, a thin, ca. 3.5 nm thick SiO_x surface layer was revealed, identified by the EELS spectra presented in Figure 4a. This is consistent with the result directly derived from HRTEM observation as shown in Figure 3c. The images in Figure 4a,b were taken along the same line across the NW at a time interval of 1 h. The Si L₂₋₃ edge characters of amor-

phous Si and SiO_x from the literature^[26] are also shown in Figure 4e and f, respectively, for comparison. We notice that the EELS spectra of the surface areas show typical SiO_x amorphous features with an L₂₋₃ edge at 103 eV for both Figure 4a and b. The thickness of the surface SiO_x layer was reduced to ca. 3.0 nm after superplastic deformation. This is in agree-

ment with the diameter reduction due to plastic necking and attributed to the surface atomic diffusion process. The shapes of the Si $L_{2,3}$ edge of the EELS spectra acquired from positions C, D and E (Fig. 4a,c) have obvious distinctive features in comparison to the spectra acquired from locations A, B and F, G. The Si $L_{2,3}$ edge of spectra C, D, and E (Fig. 4a) starts at 98 eV, which is a typical feature of crystalline Si, while the spectra C', D', and E' (Fig. 4b,d) show features of disordered Si. As revealed in the reference EELS spectra,^[26] the difference between crystalline Si and amorphous Si is not pronounced. This confirms that sp^3 bonding is preserved in the plastic-deformation-induced disordering of Si structure. We do not find any evidence of β -Sn-type phase transformations from either the electron diffraction or the EELS analysis. We also conducted in situ energy dispersive X-ray spectrometry (EDS) line scans on the Si NWs prior to and after deformation. Figure 4g,h shows the K-edge spectra from the in situ EDS line scans of silicon and elemental oxygen across the Si NW prior to and after necking deformation. There is an oxygen-rich layer in the oxygen spectra both prior to and after plastic deformation. The oxygen-rich layer is about 3 nm prior to plastic deformation, which is close to the EELS analysis results and the HRTEM observation. With plastic necking, the oxygen layer was reduced to about 2.5 nm, remaining at the same level, as shown in Figure 4h. This confirms the in situ EELS analysis results that the oxygen in the thin SiO_x layer did not diffuse along the radial direction to contribute to the initiation of dislocation plasticity and LSP of Si NWs.

From the direct atomic-scale imaging of emitted dislocations at ambient temperature in Si NWs during axial tensile experiments, we can correlate the plasticity and LSP of Si NWs with dislocation velocity and the Young's modulus. The plasticity of a particular material (i.e., whether it is brittle or ductile) is controlled by the dislocation velocity, which is regarded as the rate of emission of dislocations and/or dislocation motion. It is given by^[5]

$$v = A\tau^m \exp\left[\frac{-U}{k_B T}\right] \quad (1)$$

where v is dislocation velocity, A and m are constants, τ is shear stress, k_B is the Boltzmann constant, T is absolute temperature, and U is the activation energy of a dislocation. The activation energy can be regarded as a constant that reflects the atomic-atomic interactions and bonding characters and can be correlated to shear modulus G and elastic modulus E by $U \propto Ga_0$ and $U \propto Ea_0/[2(1+\gamma)]$,^[27-29] where a_0 is the lattice constant and γ is the Poisson ratio. The NW's surface structure differs from that of the bulk material and it strongly affects the NW's physical, chemical, and mechanical properties^[30] due to pronounced surface effects.^[31] The elastic modulus of Si is related to the size of the NW, and it decreases with decreasing NW diameter and film thickness.^[19,32] By assuming that a_0 and γ are constants, we have the simple relation

$$U_N = \frac{E_N}{E_B} U_B \quad (2)$$

where U_B and E_B are the dislocation activation energy and Young's modulus of bulk silicon, respectively, and U_N and E_N are those of the NW. Then we obtain the dislocation velocity in the NW as

$$v_N = A\tau_N^m \exp\left[\frac{-E_N U_B}{K_B k_B T}\right] \quad (3)$$

Using $U_B = 2.2$ eV^[5] and $E_B = 169$ GPa,^[19] we obtained the correlation of dislocation activation energy for the NWs U_N with the diameter of the NWs, as shown in Figure 5a; the extrapolated Si NW's Young's modulus is also plotted in the same figure. We see that the dislocation activation energy U_N decreases with decreasing NW diameter, reaching a value of 0.716 eV at a diameter of 15 nm, significantly lower than the 2.2 eV of bulk materials. We also compared the dislocation velocity for Si NWs as a function of NW diameter at room temperature. In Figure 5b the normalized dislocation velocity ratio v/v_{av} is plotted as a function of the Si NW diameter, where v_{av} is the average dislocation velocity for Si NWs. We see v increases rapidly with decreasing NW diameter. The plasticity evaluation parameter, that is, the diameter reduction ratio (Fig. 2, the star curve), is plotted in the same figure. We see that v/v_{av} shows a similar tendency to the diameter reduction ratio. This tendency demonstrates that the plasticity, that is, the diameter reduction ratio of Si NWs, is correlated with the dislocation velocity.

In summary, room-temperature LSP of single-crystalline Si NWs was directly observed by axial tensile experiments carried out in situ in an ultrahigh-resolution electron microscope. The LSP resulted in a fourfold reduction in NW diameter before fracture occurred, which is three orders of magnitude higher than that of bulk Si. The ambient temperature Si NW tensile plasticity was initiated by the emergence of a high density of dislocations, followed by the development of a continuous disordered lattice by the emission of dislocations and formation of disordered crystalline structures, before it finally became amorphous and the plastic formation of long necks occurred, which eventually resulted in fracture. The size-dependent fracture mechanism is attributed to the scale-related dislocation activities. These unusual phenomena present new fields of nanomechanics for semiconductor NWs. These discoveries also open up new applications of Si NWs in devices exposed to strain.

Experimental

Fabrication of Si NWs: A thermal evaporation technique was employed to fabricate the Si nanostructures [S1]. The evaporation source material was SiO powder. Commercial SiO was ground to a powder then put into a closed chamber, in which the Al_2O_3 substrate was located above the powder. The chamber was pumped to lower than 10 Pa. After this, 0.53×10^5 Pa of mixed Ar (90 %) and H_2 (10 %) gas was filled into the reaction chamber as the ambient gas. The graphite plate was selected as the heating material. The SiO powder was heated to about 1200 °C. The temperature of the Al_2O_3 substrate was

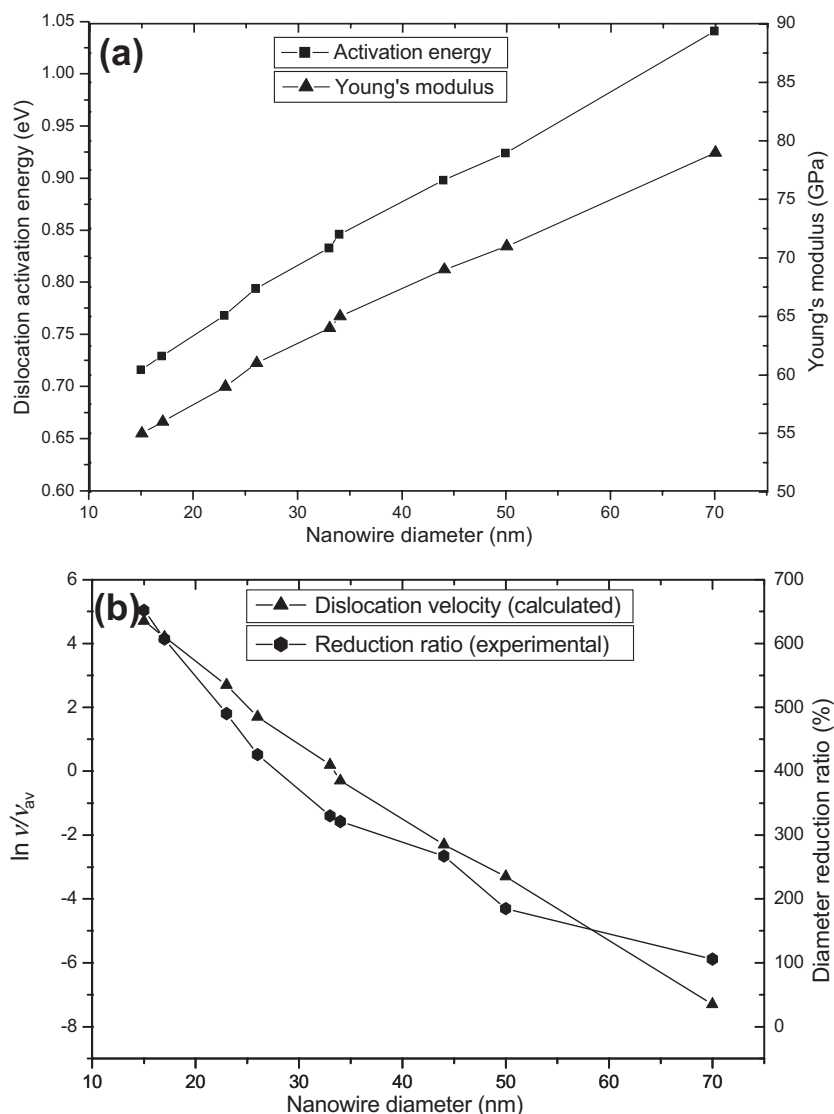


Figure 5. a) The dislocation activation energy of nanowires U_N with respect to the diameter of the nanowires. The extrapolated Si NW Young's modulus is also plotted. b) The normalized dislocation velocity ratio v/v_{av} as a function of the diameter of the Si nanowires. The diameter reduction ratio is plotted in the same figure for comparison.

about 900 °C. After the temperature had been kept at 1200 °C for 20 min, the power supply was cut off and the temperature allowed to decrease to room temperature naturally. Yellow sediments were found on the substrate. These yellow sediments, which are Si NWs with a thick SiO_x layer, were thoroughly washed with HF at room temperature. The thickness of SiO_x surface layer was effectively reduced or totally removed. Freshly made Si NWs were distributed on a TEM copper grid with colloidal/carbon supporting thin film. The general morphologies of the Si NWs are shown in Figure S1a,b. The electron diffraction analysis shown in Figure S1c demonstrates high quality Si NWs with [110] longitudinal orientation. Some of the morphologies and microstructural details of the Si NWs can be seen in [S2–S5].

Axial Tensile Testing of the Si NWs: As shown in Figure S2, a recently developed method [17,18] was used to conduct axial tensile testing of Si NWs at an ultrahigh-resolution transmission electron microscope along a particular crystallographic orientation. A copper

TEM grid with a colloidal/carbon thin film was used to apply an external mechanical driving force to deform the nanowires. The Si NW tensile tests were through *controllable* electron irradiation/heating of the specially designed celloidin/carbon supporting film on a TEM Cu grid (the colloidal/carbon supporting film must have the proper thickness). Randomly distributed nanowires occasionally bridged two (designed) broken parts of the colloidal/carbon supporting film. Upon controlled irradiation/heating by the electron beam at particular designed positions, the celloidin/carbon thin film underwent polymerization shrinkage by linear contraction of 4–5 % and pulled the Si NWs axially. The elastic modulus of the celloidin/carbon thin film is about 1–2 GPa and the Poisson ratio is 0.25–0.35.

The in situ axial-extensile experiment was conducted with two high-resolution electron microscopes. One was a regular high-resolution transmission electron microscope with LaB6 filament (JEOL 2010) and the second one was a JEOL ultrahigh-resolution scanning transmission electron microscope with a field emission gun (JEOL 2010 F). The point resolution is 0.19 nm. Both transmission electron microscopes have a 20° double tilt specimen holder and an energy dispersive X-ray spectrometer. The electron energy loss spectrometer (Model GIF200, Gatan, Pleasanton, CA) was attached to the JEOL 2010 F. Most of the axial tensile tests were conducted with the regular high-resolution transmission electron microscope with LaB6 filament. Some of the in situ UHRTEM tensile tests on the [110]-oriented Si nanowire were conducted with the JEOL 2010F to achieve atomic level resolution imaging simultaneously with the axial tensile tests to elucidate the atomistic mechanisms. During the tensile tests, the electron beam was spread to about 20–50 μm to avoid the effects of electron irradiation on the Si NWs. The operating voltage for both HRTEM observations was 200 kV and with a low electron flux dose rate around $5 \times 10^{19} \text{ e cm}^{-2} \text{ s}^{-1}$. The increased temperature of the Si NW specimens due to electron beam heating was estimated to be a few degrees above room temperature based on [S6].

Simulation of the HRTEM Images: The cubic structured Si atomic model was built with the commercial software CrystalKit and the HRTEM simulation was conducted with Mactempas. The multi-slice approximation method was used in simulating the HRTEM images. The simulated HRTEM image was obtained under the conditions of 250 Å thickness and defocus with –100 Å.

EELS and EDS Analysis: The in situ electron energy loss spectroscopy (EELS) line scan experiments were obtained using a scanning transmission electron microscope (STEM). The EELS spectra were taken using the Gatan Digitalgraph and Digiscan system with a Digiscan camera. The energy resolution was about 1.0 eV and the spatial resolution was 1.4 Å. The EELS spectra were taken across the Si nanowire diameter with a step size of 1 nm; the collection time for each spectrum was 5 s. Specimen drifting was compensated automatically. The collected raw EELS spectra were background subtracted. EDS line scan analysis was also conducted simultaneously with the HRTEM imaging and the axial tensile tests on the Si NWs.

Received: November 27, 2006
Revised: May 7, 2007
Published online: ■

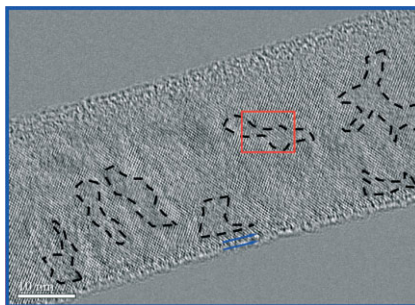
- [1] M. Born, K. Huang, *Dynamical Theory of Crystal Lattices*, Oxford University Press, Oxford **1954**.
- [2] J. R. Rice, R. Thomson, *Philos. Mag.* **1974**, *29*, 73.
- [3] U. Landman, W. D. Luedtke, N. A. Brunham, R. J. Colton, *Science* **1990**, *248*, 454.
- [4] a) J. Samuels, S. G. Roberts, *Proc. R. Soc. London A* **1989**, *421*, 1.
b) P. B. Hirsch, S. G. Roberts, J. Samuels, *Proc. R. Soc. London A* **1991**, *421*, 25.
- [5] P. B. Hirsch, S. G. Roberts, *Acta Mater.* **1996**, *44*, 2361.
- [6] G. F. Zheng, W. Lu, S. Jin, C. M. Lieber, *Adv. Mater.* **2004**, *16*, 1890.
- [7] C. Yang, Z. H. Zhong, C. M. Lieber, *Science* **2005**, *310*, 1304.
- [8] D. Tekleab, D. L. Carroll, G. G. Samsonidze, B. I. Yakobson, *Phys. Rev. B* **2001**, *64*, 035 419.
- [9] T. Cohen-Karni, L. Segev, O. Srur-Lavi, S. R. Cohen, E. Joselevich, *Nat. Nanotechnol.* **2006**, *1*, 36.
- [10] R. R. He, P. D. Yang, *Nat. Nanotechnol.* **2006**, *1*, 42.
- [11] E. W. Wong, P. E. Sheehan, C. M. Lieber, *Science* **1997**, *277*, 1971.
- [12] B. Wu, A. Heidelberg, J. J. Boland, *Nat. Mater.* **2005**, *4*, 525.
- [13] P. Poncharal, Z. L. Wang, D. Ugarte, W. A. Heer, *Science* **1999**, *283*, 1513.
- [14] J. Y. Huang, S. Chen, Z. Q. Wang, K. Kempa, Y. M. Wang, S. H. Jo, G. Chen, M. S. Dresselhaus, Z. F. Ren, *Nature* **2006**, *439*, 281.
- [15] H. D. Wagner, O. Lourie, Y. Feldman, R. Tenne, *Appl. Phys. Lett.* **1998**, *72*, 188.
- [16] M. Yu, O. Lourie, M. J. Dyer, K. Moloni, T. F. Kelly, R. S. Ruoff, *Science* **2000**, *287*, 637.
- [17] X. D. Han, Y. F. Zhang, K. Zheng, Z. Zhang, Y. J. Hao, X. Y. Guo, J. Yuan, Z. L. Wang, *Nano Lett.* **2007**, *7*, 452.
- [18] X. D. Han, Y. F. Zhang, Z. Zhang, *Chinese Patent Application 200610057989.5*, **2006**.
- [19] X. X. Li, T. Ono, Y. L. Wang, M. Esashi, *Appl. Phys. Lett.* **2003**, *83*, 3081.
- [20] D. Wang, F. H. Li, J. Zou, *Ultramicroscopy* **2000**, *85*, 131.
- [21] J. M. Cowley, A. F. Moodie, *Acta Crystallogr.* **1957**, *10*, 609.
- [22] A. George, J. Rabier, *Rev. Phys. Appl.* **1987**, *22*, 941.
- [23] S. Nakao, T. Ando, M. Shikida, K. Sato, *J. Micromech. Microeng.* **2006**, *16*, 715.
- [24] J. Z. Hu, L. D. Merkel, C. S. Menoni, I. L. Spain, *Phys. Rev. B* **1989**, *34*, 4679.
- [25] M. Menon, D. Srivastava, I. Ponomareva, L. A. Chernozatonskii, *Phys. Rev. B* **2004**, *70*, 125 313.
- [26] K. Schulmeister, W. Mader, *J. Non-Cryst. Solids* **2003**, *320*, 143.
- [27] H. Siethoff, *Phys. Status Solidi B* **2000**, *222*, 25.
- [28] M. L. Cohen, *Phys. Rev. B* **1985**, *32*, 7988.
- [29] J. C. Philips, *Bonds and Bands in Semiconductors*, Academic, New York **1973**.
- [30] R. P. Wang, G. W. Zhou, Y. L. Liu, S. H. Pan, H. Z. Zhang, D. P. Yu, Z. Zhang, *Phys. Rev. B* **2000**, *61*, 16 827.
- [31] Y. Shi, Y. S. Zhang, J. Zhu, Y. J. Yan, *Phys. Rev. Lett.* **2006**, *96*, 075 505.
- [32] M. Tabib-Azar, M. Nassirou, R. Wang, *Appl. Phys. Lett.* **2005**, *87*, 113 102.

COMMUNICATIONS

Nanowires

X. D. Han, K. Zheng,
Y. F. Zhang, X. N. Zhang,
Z. Zhang,* Z. L. Wang* ■ – ■

**Low-Temperature In Situ Large-Strain
Plasticity of Silicon Nanowires**



The large-strain plasticity (LSP) of single-crystalline silicon nanowires (Si NWs) observed in situ at room temperature by axial tension experiments carried out in an ultrahigh-resolution electron microscope is reported. The LSP is demonstrated to result in a fourfold reduction in NW diameter before fracture (see figure), which is three orders of magnitude higher than that of bulk Si.